Inventory of Error Sources Limiting GNSS-based Frequency Transfer

Ahmed Elmaghraby
Leibniz University Hannover
Institut für Erdmessung
Hannover, Germany
elmaghraby@ife.uni-hannover.de

Thomas Krawinkel
Leibniz University Hannover
Institut für Erdmessung
Hannover, Germany
krawinkel@ife.uni-hannover.de

Steffen Schön
Leibniz University Hannover
Institut für Erdmessung
Hannover, Germany
schoen@ife.uni-hannover.de

***Abstract*—Global Navigation Satellite System (GNSS) frequency transfer technique requires two GNSS receivers, each connected to an external frequency signal of the clocks or oscillator to be compared. Hence, the estimated receiver clock difference is the parameter of interest. The task is to eliminate the errors influencing the estimation process, because they degrade the stability and the uncertainty level of the transferred frequency. In this contribution, we review the most dominant error sources mentioned in literature and categorize them into hardware errors and signal propagation errors. The focus is directed further on sub-daily errors such as multipath and tropospheric delays, for which we carry out simulations of their effect on the frequency instability and the response in the frequency domain by computing the power spectrum density. Additionally, we analyze real data of two baselines with lengths of about 2 m and 295 m where all the receivers are connected to the same UTC frequency signal. The frequency instability is estimated to be in order of 10^{-17} for the first baseline and 10^{-16} for the second, where we characterize the reasons for this degradation through estimating the power spectrum of the clock difference time series.**

I. Introduction

Global Navigation Satellite Systems (GNSSs) have been widely used for time and frequency transfer (FT) because they are easy to set up and they do not require extensive infrastructure. In recent studies, GNSS FT has shown an instability level of 1×10^{-16} using Precise Point Positioning (PPP) with integer ambiguity resolution [1]. An instability range of 10^{-18} has been achieved with a zero baseline experiment by forming single differences (SDs) of carrier phase observations between two modern geodetic receivers [2]. Thanks to the elimination of most of the error sources, this experiment was done to pinpoint the limits of the GNSS receivers' hardware delays and bias fluctuations with regards to the FT application [3]. GNSS signals are prone to multiple error sources such as multipath, tropospheric delays and antenna related effects. Those errors do not cancel out when SDs of longer baselines are formed, hence the receiver clock estimation becomes more challenging. To overcome these issues and push further the limits of GNSS FT, the dominant error sources and their spatio-temporal variations should be investigated and characterized. If successful, adequate GNSS analysis procedures can be developed. Subsequently, GNSS can be used to densify chronometric leveling networks and to link remote clock locations that are not connected to an optical fibre link [4].

This study consists of two main parts. Firstly, we carry out a literature review along with simulations to address the spatio-temporal variability of the relevant error sources affecting FT instability. Each error source (alone or combined with other errors) can have a different influence on the link instability, which could be illustrated by calculating the Allan variance [5]. This gives details about the expected instability degradation in the FT link and at which averaging time it is to be anticipated. This study will expand our understanding of the GNSS FT challenges and add an essential part to our research within the framework of the Collaborative Research Center TerraQ (Relativistic and Quantum-based Geodesy). In the second part, we analyze real data of a dedicated experiment conducted at Physikalisch-Technische Bundesanstalt (PTB), Germany's national meteorology institute from April 19 to May 11, 2021. The experiment was divided into a zero-baseline and a short-baseline configuration, both of which have been discussed by [6]. In the present study, we analyze the short-baseline setup (2 m) together with a longer baseline (295 m) formed with an existing station at PTB, which is part of the International GNSS Service (IGS). The main analysis strategy is based on an SD approach using single-frequency carrier phase observations as well as ionosphere-free (IF) linear combinations of the same observations. We apply the analysis methodology on both baselines; the two-meter baseline and the longer baseline (295 m). For the latter, we expect a degradation but better use-case to assess the values acquired from the literature and the simulations.

The paper is structured as follows. Section II reviews the GNSS errors, which affect GNSS time and frequency transfer. Section III focuses on a simulation study regarding the impact of two major GNSS error sources, multipath and tropospheric delay. The PTB experiment is explained and the data analysis is presented and discussed in section IV. Section V concludes the main points of our study and gives ideas for future work.

II. Literature Review on relevant GNSS error sources

GNSS error sources influence the estimated parameters differently in terms of magnitude and time variability – yearly,

seasonally, sub-seasonally or diurnally. This depends mainly on the surrounding environment, where the required accuracy of the application determines the accepted limits of these errors. For instance, investigations have shown that the most prominent sub-seasonal GPS errors are harmonics of the GPS draconitic year [7]. The authors further discussed the sub-daily deviation in the IGS orbits focusing on sub-daily earth orientation parameter aliasing. It was also found that the weighted RMS error of the orbits provided by the IGS analysis centers for the final IGS orbit is of the order of 30–50 mm [8]. Thus, an error of 50 mm in the satellite position is equivalent to 10 mm in the station vertical component when the baseline is about 6000 km. Another study was done on IGS clock products identifying the power law stochastic processes for each GPS satellites block [9]. Our goal is to summarize and review how these errors affect the FT. We also reviewed the literature related to GNSS time transfer, because it is done using analogous technique to the FT. In both cases, the noise sources can be divided into two classes: *instrumental* and *propagation*-related errors. As for the instrumental errors, thermal noise could dominate over all other sources such as receiver tracking loop, receiver and antenna cables delay. For the signal propagation, the noise is due to fluctuations in the index of refraction of the troposphere, ionosphere and interplanetary solar plasma.

A. Hardware Instrumental Errors

The receiver and the antenna contribute to the instrumental delay. The first includes the impact of tracking loop settings, receiver cables, where antenna cables and the type of the antenna cause mainly the signal delays at the latter. A study was conducted in the frame of GNSS time transfer about the antenna delays, where a choke-ring geodetic antenna (Leica AR25) and a small pinwheel antenna (NovAtel 703-GGG) were compared [10]. The geodetic antenna showed better long-term stability than the pinwheel antenna at an averaging time of one day and a 10 ps variance at ten days, where the pinwheel antenna is limited to around 50 ps at the same averaging time. In addition, the choke-ring antenna was tested in two scenarios: once with and once without a radome where the delay due to snow was estimated to be up to 2 ns when the antenna does not have a radome. It is also noted in the same study that noise magnitude depends on the receiver's tracking loop settings. Furthermore, Ray et al. have suggested limits for the errors during time transfer with the choke-ring antenna due to the temperature sensitivity [11]. Those values may differ depending on the used antenna [12]. The limit on the antenna stability is 10.1 ps/°C for a possible long term component, where there is an upper limit of 2 ps/°C on the short term (diurnal).

The temperature affects the receiver delay as well. A temperature compensation algorithm was developed and applied to different data sets: zero, short and long baseline [13]. The modified Allan variance of the zero baseline reached the noise floor in the range of 3×10^{-17} at 1×10^{5} s averaging time after the temperature compensation, where it reached the same value at 5×10^{5} s averaging time without temperature compensation. Concerning the receiver cables, it was found that cable delay could sum up to 100 ps [14]. Therefore, calibration could be executed in some cases for GNSS signals as it is done for Galileo for time metrology purposes as presented in [15]. However, this could be crucial only for time transfer because this requires the knowledge of all electric delays of the signals inside the receiving system.

B. Signal Propagation Errors

In the signal path from the satellite to the receiver, the ionosphere and troposphere are causing significant delays to the signal, followed by multipath effects because of the antenna surroundings. Multipath and troposphere will be discussed and simulated in the following section.

Regarding the ionospheric delay effect on frequency transfer, it depends on the baseline length and it is important to note that the increase of noise in the IF linear combination can be larger with respect to the single frequency solution for short baseline [16], [17]. The ionosphere causes delay to the GNSS signal up to several tens of nanoseconds due to the electron content of the atmospheric layer, which increases during an ionospheric storm [18]. The IF linear combination of GNSS signals can remove the first order effects of the ionosphere that are proportional to signal frequency. However, there are other combinations which can remove the first, higher-order ionospheric terms plus signal path-bending effects [19]. Additionally, the satellite clocks are the most affected by the high-order ionospheric effects causing error up to 30 ps (10 mm), where the receiver and satellite positions could be affected usually by up to several millimeters [20].

The higher order ionospheric effects will not influence the FT when it is done between stations which form baselines of a couple of kilometers in length. Therefore, they shall be considered only when frequency is to be compared at intercontinental baselines as suggested in [18].

III. Simulations

In this section, we simulate the carrier phase delay caused by multipath as well as irregularities in the lower atmosphere. The latter will be investigated by computing the spectrum of the phase differences and determining the power law of the expected tropospheric fluctuations.

A. Tropospheric Fluctuations

Turbulence theory can model irregularities in the lower atmosphere [21]. This results in correlations between the carrier phase signal transmitted from one satellite to two stations on ground. There have been trials to model the temporal variations due to the troposphere in terms of populating the variance-covariance matrix to model the atmospheric fluctuations stochastically [22]. The goal is to have a physically meaningful description of the phase variations happening due to the turbulent lower atmosphere, which is crucial for precise applications. This can be simulated by the power spectrum of the phase difference when the received carrier phase signals

at two receivers are compared. The single path phase power spectrum can be modelled as

$$W_\phi(\omega) = \frac{2.192 H \sec^2\vartheta k^2 C_n^2 c a^{-\frac{5}{3}} \nu^{\frac{5}{3}}}{\left(\omega^2 + \left(\frac{k_0 \nu}{a}\right)^2\right)^{\frac{4}{3}}} \quad (1)$$

where ν is the wind velocity, k is the wave number, a is the horizontal scale factor and c is the vertical scale factor of the eddies, and ϑ is the zenith angle. Equation (1) describes the anisotropy and altitude limitation of tropospheric irregularities based on the von-Kármán spectrum of refractivity fluctuations. It is a simplified model called slab model, where the atmospheric structure constant C_n^2 and the wind speed ν are assumed to be fixed and not varying with height. The corner frequency is a function of a, ν and k_0, where $k_0 = \frac{2\pi}{L_0}$ and L_0 is the initial outer scale length of the eddies before energy dissipation [23], [24].

The phase difference power spectrum can be deducted from the signal path as follows:

$$W_{\Delta\phi}(\omega, \rho) = \text{constant} \times \frac{\sin^2\left(\frac{\omega\rho}{2\nu}\right)}{\left(\omega^2 + \left(\frac{k_0 \nu}{a}\right)^2\right)^{\frac{4}{3}}} \quad (2)$$

where the constant part depends mainly on the effective height of the tropospheric irregularities $H = 1\,\text{km}$, the wind speed $\nu = 10\,\text{m/s}$, the atmosphere structure constant $C_n^2 = 10^{-14}\,\text{m/s}^{\frac{2}{3}}$ and the elongation ratio $\frac{a}{c} = 100$. For our simulations, we used those parameter values derived from the literature. The $\sin^2(\cdot)$ term depends on the interference pattern of the receivers, and it depends only on the inter-receiver distance ρ and the wind speed ν.

As shown in Figure 1, equation (2) is simulated with additive white Gaussian noise appearing in the high frequencies. This spectrum indicates clearly the expected behavior through power law distributions as a result of the turbulent atmosphere. The spectrum before the corner frequency shows a slope of $\omega^{-\frac{2}{3}}$, and afterward the slope is $\omega^{-\frac{8}{3}}$.

B. Multipath

Due to reflectors surrounding the antenna, GNSS signal may arrive at the antenna from different paths other than the direct path from the satellite. Those non-line-of-sight signals experience phase delay and magnitude attenuation, hence add to the direct signal influencing the signal acquisition at the receiver. The multipath error has been simulated here for the carrier phase measurements. The formula used has been developed in previous work [25], [26]:

$$\delta\phi = \tan^{-1}\left(\frac{\alpha \sin(\Delta\phi_R)}{1 + \alpha\cos(\Delta\phi_R)}\right) \quad (3)$$

where $0 \leq \alpha \leq 1$ is the amplitude ratio between the direct and the reflected signal, i.e. the attenuation factor and it depends on the electrical permittivity ϵ and the magnetic permeability

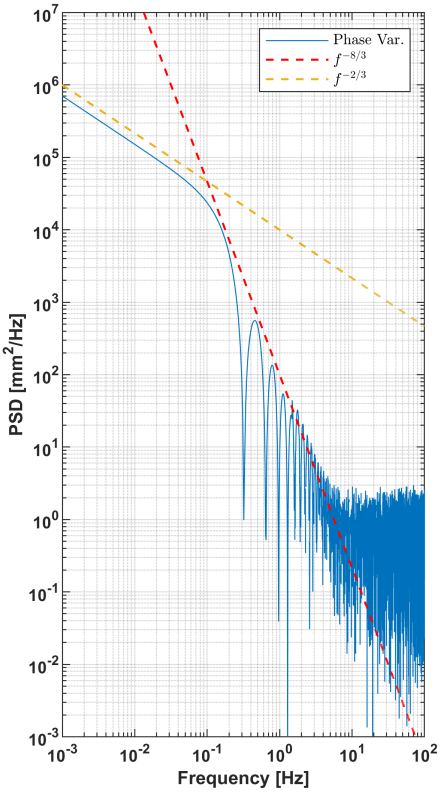

Fig. 1. Simulated phase variations spectrum with white noise

μ of the reflector [27]. The reflected signal phase shift $\Delta\phi_R$ from the direct signal (extra path delay) can be computed by

$$\Delta\phi_R = \frac{4\pi h}{\lambda}\sin(\epsilon) \quad (4)$$

It depends on the antenna monument height h and the satellite elevation angle ϵ.

In Figure 2, we simulate the extra path delay $\delta\phi$ for elevation angle varies from 15° to 90° and two antenna monument height values $h = 0.5\,\text{m}$ and $h = 2.0\,\text{m}$. For both cases, we choose $\lambda = 0.19\,\text{m}$ which is the wavelength of the GPS L1 signal and the attenuation value has been chosen to be $\alpha = 0.06$. It is assumed that the reflecting surface is horizontal and infinite. The data is generated for almost four hours, which represents an average satellite pass with a sampling of 0.5°. We can notice that the fluctuations due to multipath increases with lower elevation angles and

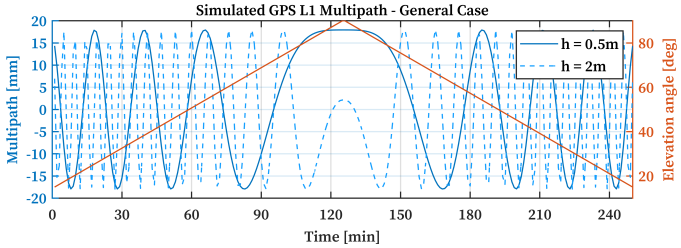

Fig. 2. Multipath simulation for different monument heights

its frequency increases with the monument height for the same attenuation factor. We extend then the same methodology to simulate the multipath error for 24 hours and we use the elevation angles from real data representing the available constellation acquired at one station (PTBB) on May 10, 2021 during our experiment at PTB. The path delay has been estimated for each satellite pass, then the results have been averaged for each epoch accordingly. The time series is depicted by Figure 3. We then estimate the spectrum of this time series by computing its periodogram. Figure 4 illustrates the slope of flicker noise which is -1, and the energy in the frequency band from 10^{-3} Hz to 10^{-2} Hz.

IV. Data Analysis

A. Experiment Setup

The experiment was conducted in a short-baseline configuration from May 1 to May 10, 2021. For this experiment, we use two geodetic receivers (Septentrio PolaRx5TR), which were connected to the same frequency signal of the locally generated approximation of Coordinated Universal Time (UTC), referred to as UTC(PTB). To set up the short baseline experiment, we connected each receiver to separate antennas of the same type (Leica AR20) that were installed approximately two meters apart as illustrated in Figure 5. The signal paths from the antenna to each receiver were identical to ensure identical delays. Those two antennas were located at the Meitner building and they formed two stations referred to as MEI1 and MEI2. For a longer baseline, we used the PTBB station that is located at the Kopfermann building at PTB premises. That station is equipped with a Leica AR25 antenna and a Septentrio PolaRx5TR receiver which is connected to the UTC(PTB) signal as well. The baseline (PTBB-MEI1) amounts to approximately 295 m. Table I includes the topocentric coordinate difference of PTBB and MEI1 which are computed considering MEI2 to be the reference station.

B. Processing

The single frequency carrier phase observables are used to estimate the relative clock error between the available receivers. We process the GPS signals L1(C/A), L2W, L2C and L5, as well as the Galileo signals E1, E5a and E5a+b. Beside that, we compute the IF linear combination forming

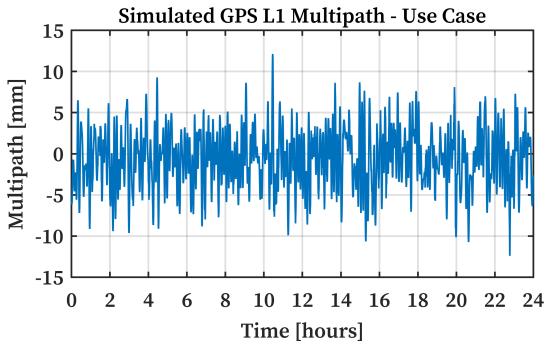

Fig. 3. Simulated GPS L1 multipath for all satellites visible at a PTB station

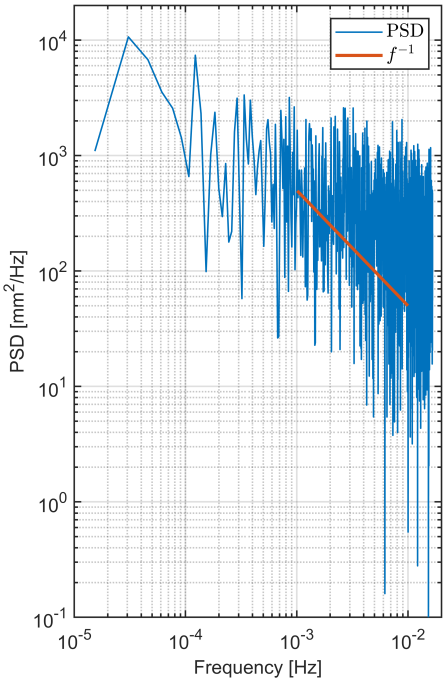

Fig. 4. Periodogram of the simulated GPS L1 multipath error from Figure 3

TABLE I
Station Coordinates in Topocentric Reference Frame

Station	North [m]	East [m]	Up [m]
PTBB	−27.753	−290.722	−16.090
MEI1	0.450	1.984	0.003

GPS L1C-L2(W-C), GPS L1C-L5Q, Galileo L1C-L5Q and Galileo L1C-L8Q. For clarification, Table II lists the signals and their corresponding naming in RINEX 3 format [28]. The RINEX files have been generated with sampling interval of 30 seconds.

As pre-processing configuration we apply elevation cut-off angle of 15°, identity weighting matrix, minimum C/N_0

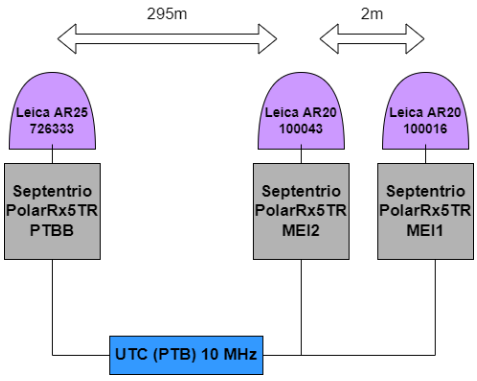

Fig. 5. Measurement setup diagram

TABLE II
RINEX SIGNAL NAMING

Designation	Signal
GL1C	L1(C/A)
GL2W	L2 P-code
GL2C	L2C
GL5Q	L5
EL1C	E1
EL5Q	E5a
EL58	E5(a+b)

20 dB-Hz and minimum arc length of 300 s. In order to eliminate the outliers, we choose the carrier phase threshold to be 0.1 cycle for the MEI1-MEI2 baseline and 0.5 cycle for the PTBB-MEI1 baseline. In addition, we use satellite orbit and clock products from the Centre of Orbit Determination in Europe (CODE) provided within the framework of the Multi-GNSS Experiment (MGEX) of the International GNSS Service (IGS)[29]. Carrier phase observations are corrected for the phase wind-up effect as well as phase center offsets and variations derived from the correction data provided by the IGS14 model [30]. Tidal and loading effects are applied according to the IERS 2010 conventions [31]. For each baseline, we compute the receiver-to-receiver single differences following the common view approach.

Afterwards, the least-squares adjustment has been implemented to estimate the relative clock error between the two receivers after applying the single differences [32], [33]. The estimated parameters vector includes the relative position between the two receivers ($\Delta x, \Delta y, \Delta z$), and the relative clock error (δt). In our case we estimate however only the relative clock error as the stations coordinates are already known and we process data from the baselines less than a couple of kilometers. Finally, we use the modified Allan deviation (MDEV) to characterize the frequency instability of each time series. The slope of the expected white phase modulation noise (WPM) is also depicted as reference.

C. Results

Tables III and IV present the standard deviation of the processed observables in both cases, the single frequency and IF linear combination, respectively. The MDEV has been chosen over standard Allan deviation, because it can differentiate between white phase modulation noise and flicker phase modulation noise [34]. We compute the power spectrum density of the relative clock error time series estimated for three signals: GPS L2W and L2C, and Galileo E5a. Because the stochastic process is formed by the power law distribution, which in turn can be described using the power spectral density function, the periodogram has been used to estimate the power spectrum density [35]. We choose a window size of 256-point to average the total number of samples during our ten-day PTB experiment, where the sampling rate is 30 s so we have 2,880 epochs per day. This also means that there are 28,800 samples for the corresponding time series. We apply

TABLE III
STANDARD DEVIATION OF VARIOUS MEAN SINGLE FREQUENCY SINGLE DIFFERENCES FOR BOTH MEASUREMENT CONFIGURATIONS

Configuration	Observation types	STD [mm]
MEI1-MEI2 (2m)	GPS L1C	1.0
	GPS L2W	1.2
	GPS L2C	1.5
	GPS L5Q	1.6
	Galileo E5a	1.3
	Galileo E5(a+b)	1.1
PTBB-MEI1 (295m)	GPS L1C	6.0
	GPS L2W	5.9
	GPS L2C	5.8
	GPS L5Q	6.1
	Galileo E5a	6.2
	Galileo E5(a+b)	5.7

TABLE IV
STANDARD DEVIATION OF IONOSPHERE-FREE SINGLE DIFFERENCES FOR BOTH MEASUREMENT CONFIGURATIONS

Configuration	Observation types	STD [mm]
MEI1-MEI2 (2m)	GPS L1/L2W	2.4
	GPS L1/L2C	3.1
	GPS L1/L5Q	3.1
	Galileo E1/E5a	2.5
	Galileo E1/E5(a+b)	2.4
PTBB-MEI1 (295m)	GPS L1/L2W	6.0
	GPS L1/L2C	6.4
	GPS L1/L5Q	6.4
	Galileo E1/E5a	6.1
	Galileo E1/E5(a+b)	6.0

thus the periodogram to have better localization of the signal components in the frequency domain. Additionally, we search for specific slopes to define the errors causing deviation and larger instability. We plotted the slopes of various noise processes as learned from literature because this makes it easier to define error sources and test the periodogram estimation process accordingly.

1) Single Frequency: Figure 6 shows the MDEV for both baselines. For the MEI1-MEI2 baseline, we can see that it reaches the flicker noise after one day averaging with instability values of 10^{-17}. Where the frequency instability is degraded by one order of magnitude reaching only 10^{-16} for the PTBB-MEI1 at the same averaging period as shown in Figure 6b. This is mainly because of remaining uncorrelated errors such as multipath.

For GPS signals (L2W, L2C), the periodogram has been computed and plotted for two different baselines in logarithmic scale. As shown in figures 7e and 7f, the slope is between $\frac{-8}{3}$ and $\frac{-2}{3}$ at first, and then saturates with a zero-slope at high frequencies. The first part could be evidence of non-compensated tropospheric delays or fluctuations [21], where the white noise (zero-slope) shows the magnitude of the error as a result of the thermal and instrumental noise. As for

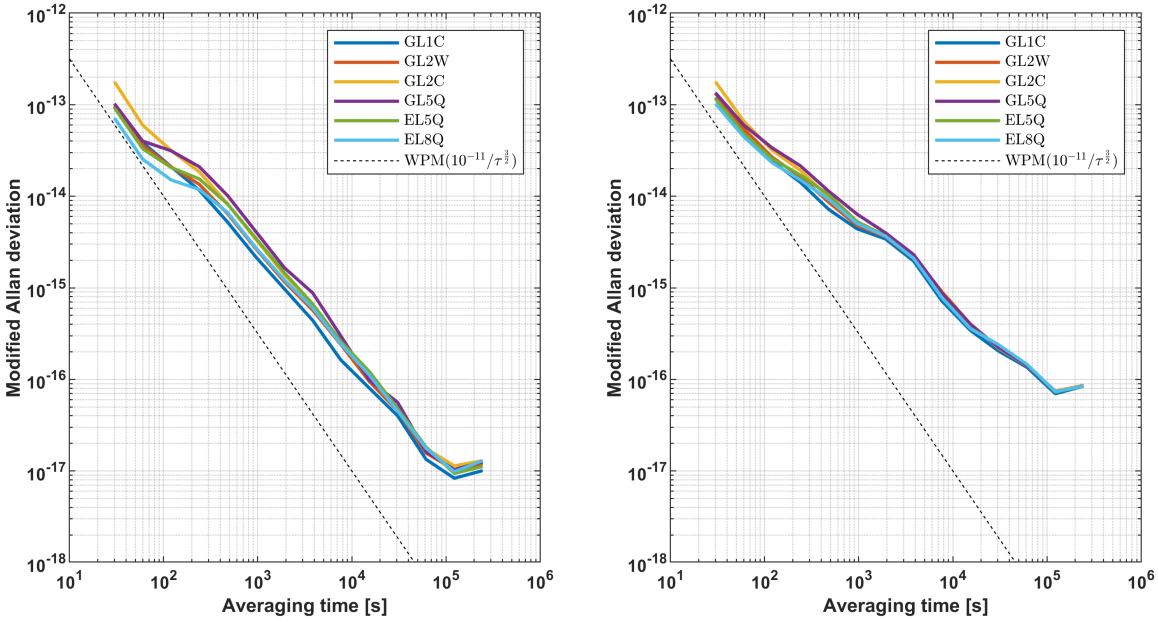

(a) Single frequency, 2 m

(b) Single frequency, 295 m

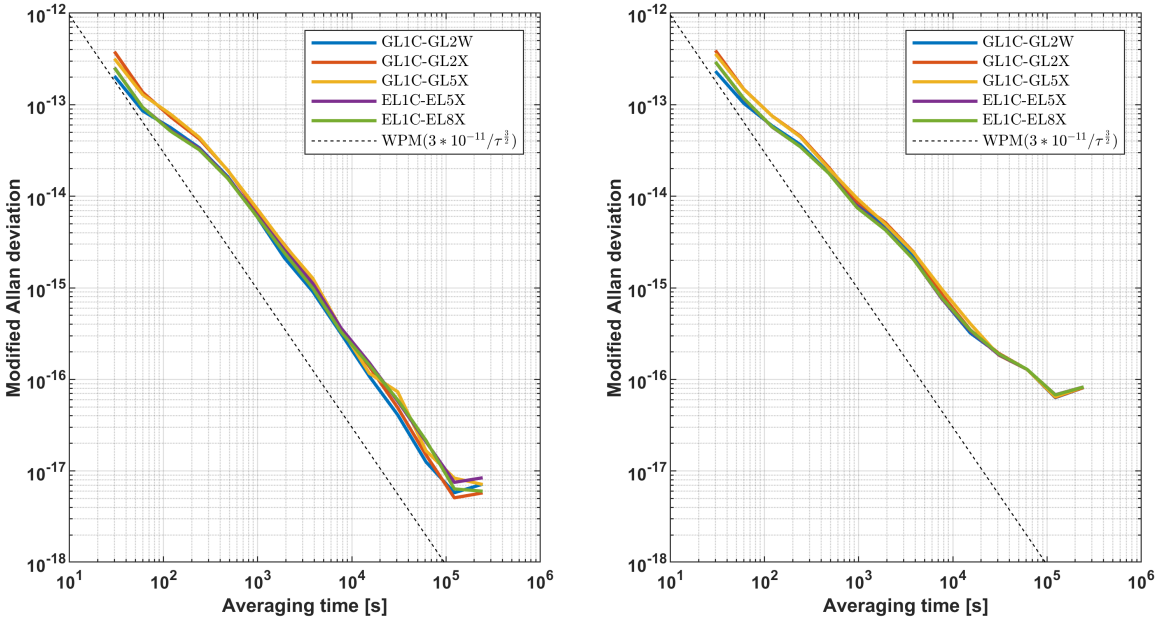

(c) IF linear combination, 2 m

(d) IF linear combination, 295 m

Fig. 6. Modified Allan deviations for baselines MEI1-MEI2 and PTBB-MEI1

figures 7a, 7b and 7c, the periodogram does not show a similar slope as the baseline is only 2 m long. This is expected because applying single differences should eliminate virtually all the errors including the similar tropospheric delay at both receivers. However, we find the same white noise (zero-slope) share, and with its corresponding amplitude depending on the hardware delay at the receivers, cables and the temperature fluctuations.

2) Ionosphere-free Linear Combination: As illustrated in figures 6c and 6d, the results show a slightly worse short-term instability, where the variance of the time series is almost three times the variance of the single-frequency case as mentioned in Tables III and IV for the MEI1-MEI2 baseline. However, this is not the case for the PTBB-MEI1 baseline as the standard deviation of the IF linear combination is the same or slightly higher than that of the single-frequency case. The reason for this could be the height difference between stations PTBB and MEI1 which amounts to about 16 meters as listed in Table I, hence it dominates the systematic noise expected by forming the IF linear combination.

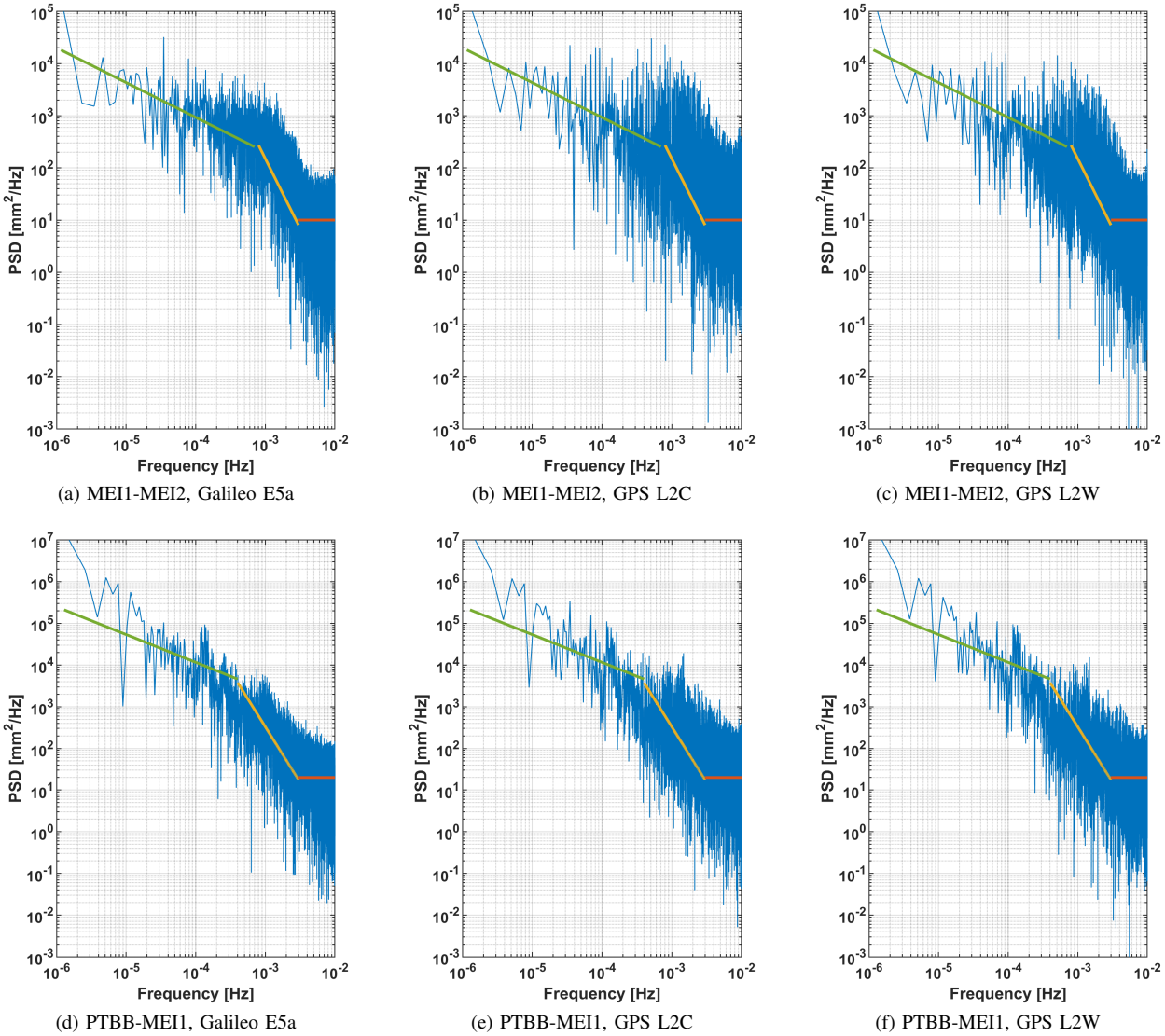

(a) MEI1-MEI2, Galileo E5a (b) MEI1-MEI2, GPS L2C (c) MEI1-MEI2, GPS L2W

(d) PTBB-MEI1, Galileo E5a (e) PTBB-MEI1, GPS L2C (f) PTBB-MEI1, GPS L2W

Fig. 7. Power Spectrum: a power law x^k where $k = -\frac{2}{3}$ (green), $k = -\frac{8}{3}$ (yellow), $k = 0$ (orange)

V. Conclusions

In this paper, we collected dominant error sources influencing the GNSS-based time and frequency transfer based on literature review. Simulations have been carried out to characterize the impact of the carrier phase variations due to multipath and troposphere. The effect of multipath is in the order of millimeters. The larger the monument height, the higher the frequency of the phase fluctuations. A power law behavior is used to simulate the phase variations due to the tropospheric irregularities according to turbulence theory. This suggests a potential tropospheric delay compensation by estimating the time correlations of the received phase at the two stations. Furthermore, the spectrum of the estimated time series has shown power law slopes of $-\frac{8}{3}$ to $-\frac{2}{3}$ agreeing with the simulations done based on turbulence theory. The relation to the turbulence theory requires further investigation with longer baselines where the tropospheric effect becomes more evident.

A link instability below 1.5×10^{-17} for the two-meter baseline after one day averaging time was obtained, where the values are degraded to 1×10^{-16} when the same methodology is extended on the longer baseline (295 m) using single differences algorithms. The computation of the power spectrum also gives the possibility to determine the behavior of the various errors in the frequency domain and their power law distribution. Whereas the modified Allan deviation shows degradation of the instability with longer baseline in the time domain, the spectrum indicates different slopes which may correspond to different noise processes in the frequency domain. More detailed simulations are planned in future, along with real data analysis. This shall contribute to modeling the error sources rigorously reducing the GNSS FT uncertainty to values lower than 5×10^{-17}. Therefore, we will predicate on

our findings in this study to develop the correction concepts and implement them into our software. This will complete the knowledge of the limitations of GNSS FT and will help us to proceed with the future chronometric leveling campaigns to reach centimeter resolution between locations of geodetic interest.

Acknowledgment

The authors would like to thank Dr. Andreas Bauch and his team at PTB for their assistance and support in preparing, conducting and analyzing the experiment. This research was funded by the Deutsche Forschungsgemeinschaft (DFG, German Research Foundation) – project number 434617780 – SFB 1464.

Disclaimer

The authors do not attempt to recommend any of the instruments under test. It is noted that the performance of the equipment presented in this paper depends on the particular environment and the individual instruments in use. Other instruments of the same type or the same manufacturer may show different behavior. The readers are, however, encouraged to test their own equipment to identify the system performance with respect to a particular application.

References

[1] G. Petit and P. Defraigne, "The performance of GPS time and frequency transfer: Comment on 'A detailed comparison of two continuous GPS carrier-phase time transfer techniques'," *Metrologia*, vol. 53, pp. 1003–1008, 2016. DOI: 10.1088/0026-1394/53/3/1003.

[2] T. Krawinkel, S. Schön, and A. Bauch, "Recent and Future Activities at Leibniz University Hannover in GNSS Frequency Transfer," in *2021 Joint Conference of the European Frequency and Time Forum and IEEE International Frequency Control Symposium (EFTF/IFCS)*, 2021. DOI: 10.1109/EFTF/IFCS52194.2021.9604309.

[3] U. Weinbach, S. Schön, and T. Feldmann, "Evaluation of state-of-the-art geodetic GPS receivers for frequency comparisons," in *IEEE International Frequency Control Symposium Joint with the 22nd European Frequency and Time Forum*, 2009, pp. 263–268. DOI: 10.1109/FREQ.2009.5168182.

[4] H. Denker, L. Timmen, C. Voigt, *et al.*, "Geodetic methods to determine the relativistic redshift at the level of 10^{-18} in the context of international timescales: a review and practical results," *Journal of Geodesy*, vol. 92, no. 5, pp. 487–516, 2018. DOI: 10.1007/s00190-017-1075-1.

[5] D. W. Allan, "Time and Frequency (Time-Domain) Characterization, Estimation, and Prediction of Precision Clocks and Oscillators," *IEEE Transactions on Ultrasonics, Ferroelectrics and Frequency Control*, vol. 34, no. 6, pp. 647–654, 1987.

[6] T. Krawinkel, A. Elmaghraby, and S. Schön, "Exploring the Technical Limits of GNSS-based Frequency Transfe," *Proceedings of the 53rd Annual Precise Time and Time Interval Systems and Applications Meeting*, pp. 188–198, 2022. DOI: 10.33012/2022.18288.

[7] J. Griffiths and J. R. Ray, "Sub-daily alias and draconitic errors in the IGS orbits," *GPS Solutions*, vol. 17, no. 3, pp. 413–422, 2013. DOI: 10.1007/s10291-012-0289-1.

[8] R. Dach, G. Beutler, U. Hugentobler, *et al.*, "Time transfer using GPS carrier phase: error propagation and results," *Journal of Geodesy*, vol. 77, no. 1-2, pp. 1–14, 2003. DOI: 10.1007/s00190-002-0296-z.

[9] K. L. Senior, J. R. Ray, and R. L. Beard, "Characterization of periodic variations in the GPS satellite clocks," *GPS Solutions*, vol. 12, no. 3, pp. 211–225, 2008. DOI: 10.1007/s10291-008-0089-9.

[10] P. Defraigne, E. Pinat, B. Bertrand, *et al.*, "Stability of Hardware Delays of GNSS Signals," 2021. DOI: 10.1109/EFTF/IFCS52194.2021.9604324.

[11] J. Ray and K. Senior, "Geodetic techniques for time and frequency comparisons using GPS phase and code measurements," *Metrologia*, vol. 42, no. 4, pp. 215–232, 2005. DOI: 10.1088/0026-1394/42/4/005.

[12] J. R. Ray and K. Senior, "Temperature Sensitivity of Timing Measurements Using Dorne Margolin Antennas," *GPS Solutions*, vol. 5, no. 1, pp. 24–30, 2001. DOI: 10.1007/PL00012873.

[13] D. G. Enzer, D. W. Murphy, and W. A. Diener, "Frequency Comparisons via GPS Carrier-phase: Jump Processing, Temperature Compensation and Zero/Short-baseline Noise-floors," in *Proceedings of the 50th Annual Precise Time and Time Interval Systems and Applications Meeting*, Institute of Navigation, 2019, pp. 68–82. DOI: 10.33012/2019.16744.

[14] C. Rieck, P. Jarlemark, K. Jaldehag, and J. Johansson, "Thermal influence on the receiver chain of GPS carrier phase equipment for time and frequency transfer," in *Proceedings of the 2003 IEEE International Frequency Control Symposium and PDA Exhibition Jointly with the 17th European Frequency and Time Forum*, 2003, pp. 326–331. DOI: 10.1109/FREQ.2003.1275110.

[15] P. Defraigne, W. Aerts, G. Cerretto, E. Cantoni, and J.-M. Sleewaegen, "Calibration of Galileo signals for Time Metrology," *IEEE Transactions on Ultrasonics, Ferroelectrics, and Frequency Control*, vol. 61, no. 12, pp. 1967–1975, 2014. DOI: 10.1109/TUFFC.2014.006649.

[16] P. Defraigne and K. Verhasselt, "Multi-GNSS Time Transfer with CGGTTS-V2E," in *2018 European Frequency and Time Forum (EFTF)*, 2018, pp. 270–275. DOI: 10.1109/EFTF.2018.8409047.

[17] G. D. Rovera, M. Abgrall, P. Uhrich, P. Defraigne, and B. Bertrand, "GNSS antenna multipath effects," in *2018 European Frequency and Time Forum (EFTF)*, 2018, pp. 208–212. DOI: 10.1109/EFTF.2018.8409034.

[18] S. Pireaux, P. Defraigne, L. Wauters, *et al.*, "Higher-order ionospheric effects in GPS time and frequency transfer," *GPS Solutions*, vol. 14, no. 3, pp. 267–277, 2010. DOI: 10.1007/s10291-009-0152-1.

[19] S. Bassiri and G. A. Hajj, "Higher-order ionospheric effects on the GPS observables and means of modeling them," *Manuscripta Geodaetica*, vol. 18, no. 6, pp. 280–289, 1993.

[20] M. Hernández-Pajares, J. M. Juan, J. Sanz, and R. Orús, "Second-order ionospheric term in GPS: Implementation and impact on geodetic estimates," *Journal of Geophysical Research: Solid Earth*, vol. 112, no. B8, 2007. DOI: 10.1029/2006JB004707.

[21] A. D. Wheelon, "The temporal variation of phase," in *Electromagnetic Scintillation*. Cambridge University Press, 2001, vol. 1, pp. 240–316. DOI: 10.1017/CBO9780511534805.007.

[22] S. Schön and F. K. Brunner, "Atmospheric turbulence theory applied to GPS carrier-phase data," *Journal of Geodesy*, vol. 82, no. 1, pp. 47–57, 2008. DOI: 10.1007/s00190-007-0156-y.

[23] T. Nilsson, J. Böhm, D. D. Wijaya, *et al.*, "Path Delays in the Neutral Atmosphere," in *Atmospheric Effects in Space Geodesy*, J. Böhm and H. Schuh, Eds., Springer, 2013, pp. 73–136. DOI: 10.1007/978-3-642-36932-2_3.

[24] G. Kermarrec and S. Schön, "On the determination of the atmospheric outer scale length of turbulence using GPS phase

difference observations: the Seewinkel network," *Earth, Planets and Space*, vol. 72, no. 1, pp. 1–16, 2020.

[25] C. Rost and L. Wanninger, "Carrier phase multipath corrections based on GNSS signal quality measurements to improve CORS observations," in *IEEE/ION Position, Location and Navigation Symposium*, 2010, pp. 1162–1167. DOI: 10.1109/PLANS.2010.5507235.

[26] M. Smyrnaios, S. Schn, M. Liso, and S. Jin, "Multipath propagation, characterization and modeling in GNSS," *Geodetic sciences-observations, modeling and applications*, pp. 99–125, 2013.

[27] F. Dilssner, G. Seeber, G. Wuebbena, and M. Schmitz, "Impact of Near-Field Effects on the GNSS Position Solution," in *Proceedings of the 21st International Technical Meeting of the Satellite Division of The Institute of Navigation*, 2008, pp. 612–624.

[28] W. Gurtner and L. Estey, *RINEX: The Receiver Independent Exchange Format Version 3.00*, 2007. [Online]. Available: https://files.igs.org/pub/data/format/rinex300.pdf (visited on 05/18/2022).

[29] O. Montenbruck, P. Steigenberger, L. Prange, *et al.*, "The Multi-GNSS Experiment (MGEX) of the International GNSS Service (IGS) - Achievements, prospects and challenges," *Advances in Space Research*, vol. 59, no. 7, pp. 1671–1697, 2017. DOI: 10.1016/j.asr.2017.01.011.

[30] G. Beyerle, "Carrier phase wind-up in GPS reflectometry," *GPS Solutions*, vol. 13, no. 3, pp. 191–198, 2009. DOI: 10.1007/s10291-008-0112-1.

[31] G. Petit and B. Luzum, Eds., *IERS Conventions (2010)*, ser. IERS Technical Note. Frankfurt am Main: Verlag des Bundesamts für Kartographie und Geodäsie, 2010, vol. 36.

[32] G. Blewitt, "Basics of the GPS Technique: Observation Equations," in *Geodetic Applications of GPS*, B. Johnson, Ed., Nordic Geodetic Commission, Sweden, 1997.

[33] A. Leick, L. Rapoport, and D. Tatarnikov, "GNSS Positioning Approaches," in *GPS Satellite Surveying*, A. Leick, D. Tatarnikov, and L. Rapoport, Eds., Wiley, 2015, pp. 257–399. DOI: 10.1002/9781119018612.ch6.

[34] W. J. Riley, *Handbook of Frequency Stability Analysis*, ser. Special Publication (NIST SP) 1065. 2008.

[35] F. Auger and P. Flandrin, "Improving the Readability of Time-Frequency and Time-Scale Representations by the Reassignment Method," *IEEE Transactions on Signal Processing*, vol. 43, no. 5, pp. 1068–1089, 1995. DOI: 10.1109/78.382394.